Structure dependence of molecular reactions on surfaces

Cao, K.

Chapter 2

Experimental apparatus and techniques

2.1 Ultra-high vacuum apparatus

2.1.1 Potvis

Potvis is a home-built UHV system with a base pressure below 8×10^{-11} mbar. This system contains a double differential-pumping supersonic molecular beam chamber, a quadrupole mass spectrometer (QMS, Pfeiffer QMA 200), a quadrupole mass spectrometer (QMS, Pfeiffer QMA 400) which can move along themolecular beam axis, and a LEED/AES (OCI BDL800IR-MCP) system.

The main UHV chamber is connected to a series of 3 vacuum chambers used to generate a well-defined molecular beam through supersonic expansion of gases. The molecular beam is generated by expansion of a gas (or a gas mixture) at a total pressure of $1.0 \sim 5.0$ bar through a tungsten nozzle with a 25 μm diameter orifice. The nozzle's 25 μm diameter orifice is accurately positioned at variable distance (between approx. 1 and 15 mm) from the first of this series of skimmers (Model 1, 0.25 mm, Beam Dynamics). To increase the kinetic energy of molecules in the expansion, the tungsten tip of the nozzle is heated radiatively by a second short tungsten tube that surrounds the tungsten tip. This second tube is heated by electron bombardment using two oppositely positioned filaments. A C-type thermocouple is spot-welded to the Ta part of the expansion tube, approx. 10-20 mm from the 25 μm diameter orifice.

We skim the gas expansion in the source chamber to create a beam which passes through two stages of differential-pumping prior to entering the UHV chamber, which houses a temperature-controlled single crystal on an *x, y, z, θ* manipulator. A valve separates the two differential pumping stages. Two additional flags in the beam line can be opened and closed. They are used to determine the absolute dissociation probabilities by the King and Wells (KW) technique[10]. The first flag is located in the first differential pumping stage. The second flag is located inside the main UHV chamber. The opening and closing of both flags is computer-controlled to ensure an accurate timing. For KW measurements, we use a Baltzers quadrupole mass analyzer (QMA 200), positioned such that it samples the pressure rise from the SMB after equilibration inside the chamber. When retracting the sample, the beam enters the differentially-pumped housing of a Baltzer's 400 quadrupole mass analyzer (QMA 400) of a special linear design with a cross-beam ionizer and two consecutive quadrupole mass filters. It is used to determine the kinetic energy of molecules in the beam through time-of-flight (TOF) analysis and for temperature programmed desorption (TPD). The differentially-pumped QMA is retractable over 200 mm along the beam axis, allowing TOF measurements for varying neutral flight path lengths. More details of our entire UHV-SMB system were previously described in Ref.[11].

2.1.2 Lionfish

Lionfish is another home-build ultra high vacuum (UHV) apparatus (base pressure is below 1×10^{-10} mbar). This system contains a double differential-pumping super sonic molecular beam chamber, a quadrupole mass spectrometer (QMS, Pfeiffer QMA 200), a quadrupole mass spectrometer (UTI, 100C) which can move along the molecular beam axis, and a LEED/AES (OCI BDL800IR-MCP) apparatus.

The crystal is mounted on an x, y, z, θ manipulator. The surface temperature can be controlled between 89 and 1300 K with the use of liquid nitrogen cooling and radiative heating combined with electron bombardment for heating.

The molecular beam is generated by expansion of a gas (or a gas mixture) at a total pressure of $1.0 \sim 4.0$ bar through a tungsten nozzle with a 28 μm diameter orifice. The beam is shaped by two skimmers (subsequent diameters from the expansion nozzle are 0.45 mm and 2.5

mm). Two flags, one positioned in the second differential pumping chamber and one in the UHV chamber, and a chopper wheel located in the first differential chamber, modulate the beam. The two flags are used to determine the absolute dissociation probability using the King and Wells (KW) technique[10]. The chopper wheel is a fast rotating disk (∼250 Hz) with two broad (17 mm) and two narrow (0.85 mm) slits. It is used to determine the kinetic energy and the energy distribution using time-of-flight (TOF) techniques.

A home-made gate valve separates the second differential pumping chamber and the UHV chamber. It consists of a rectangular plate with four orifices. It slides through a groove cut into a solid flange with knife edges on both sides. A linear feedthrough accurately positions the sliding plate within the groove. The sliding plate contains, besides an O-ring to seal the UHV chamber, one larger hole with a diameter of 6.2 mm, one medium-sized hole with diameter of 3.2 mm, one small hole with diameter of 1.6 mm, and a rectangular slit of 3.2 mm in horizontal direction and 0.065 mm in vertical direction. By choosing different orifices on the plate, we can change the molecular beam's size and shape at the crystal position inside the UHV chamber.

2.2 Experimental techniques

2.2.1 Low energy electron diffraction

Low energy electron diffraction (LEED) is a technique to study surface structures. The rather simple and well known example for diffraction is Bragg diffraction:

$$2dsin\theta = n\lambda \tag{2.1}$$

where d is the interplanar distance, θ is the scattering angle, n is a positive integer and λ is the wavelength, in the present case of the electron beam. Scattering the electron beam from the surface will yield a pattern with spots, showing the crystal in reciprocal space.

For a surface containing steps, the following expression for the scattered intensity I at an angle φ is derived[12]:

$$I(\varphi) = const. \frac{sin^2[\frac{1}{2}ka(N+1)sin\varphi]}{sin^2[\frac{1}{2}kasin\varphi]} \times \sum_{i=-\infty}^{+\infty} \delta[\frac{1}{2}k(N \times a + g)sin\varphi + \frac{1}{2}kd(1+cos\varphi) - i\pi] \tag{2.2}$$

where I is the intensity of electron beam in direction φ, $k = 2\pi/\lambda$, λ is the wavelength of the electron beam, $N+1$ is the number of atom rows on one terrace and a is the separation of atom rows, d is the step height and g is the horizontal shift of the top layer compared with the adjacent step, i is an integer.

The first term of equation 2.2 is due to the finite number of atoms on a single terrace and equals the expression for the intensity distribution for a grating with $N+1$ slits. The second term of equation 2.2 is a sum of δ-functions in the limit of an infinite number of steps. The figure 2.1 shows simulations of LEED for $Pt[N(111) \times (100)]$ surfaces at two different beam energies. The (0,0) spot is a single spot at beam energy equals 65.7 eV and becomes doublet at 89.5 eV. As the right panel shows, the spot splitting decreases with increasing the terrace length N.

For $(0,0)$ spot, $\varphi = 0$, the second term of equation 2.2 can be rewritten as the following equation by using $\lambda \sim \sqrt{150/V}$, where V is the acceleration voltage of the electron beam:

$$V_{00} = \frac{150i^2}{4d^2} \tag{2.3}$$

where V_{00} is the voltage in volts for observation of a single $(0,0)$ spot, d is the step height in Å. For a integral i the $(0,0)$ spot is a single spot. The value $E = 65.7eV$ in the left panel of figure 2.1 corresponds to $i = 3$. To get a doublet with equal intensity in each spot, two delta functions that lie symmetrical on both sides near $(0,0)$ are required. This responds to the half-integer value of i. The energy 89.5 eV in the right panel of figure 2.1 corresponds to $i = 3.5$. By measuring the voltages corresponding to single or doublet spots of $(0,0)$ and combining with equation 2.3, the step height can be obtained.

The LEED patterns in this thesis are obtained using a microchannel plate (MCP) LEED/AES optics (OCI BDL800IR-MCP). Because of the design of this LEED system, the patterns are distorted. The details

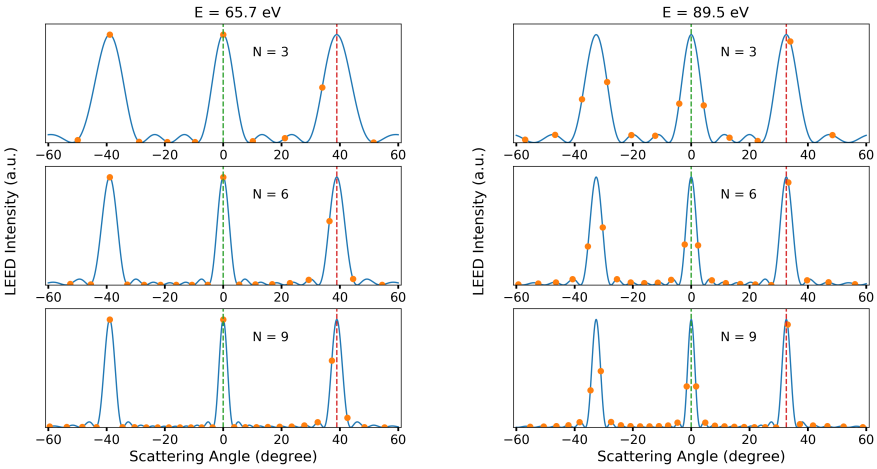

Figure 2.1: The simulation of LEED by using equation 2.2. The parameters used are from a series of $Pt[N(111) \times (100)]$ surfaces, where a is 2.40 Å, d is 2.27 Å and g is 1.60 Å. The beam energies are 65.7 eV and 89.5 eV for left and right figures, respectively. The solid curves are from the first term of equation 2.2. The circles are from the second term of equation 2.2.

of the origin of distortions and the correction procedures are described in Ref. [13].

2.2.2 King and Wells technique

The sticking probability of a molecule on a single crystal surface is measured directly by the King and Wells (KW) technique[10]. It requires two flags on the beam axis. One is positioned in the beam line prior to it entering the UHV chamber. The second flag is inside the UHV chamber and can block the beam from impinging onto the crystal. The measurement consists of the follow steps:

- At the beginning, both of the flags are closed. The beam is blocked from entering the UHV chamber. The QMS measures the effusive load of the beam.

- First, the first flag in the beam line is opened. The beam enters into the UHV chamber but does not collides with the surface, because the second flag is closed. This will cause a rise of the QMS intensity, labeled as L_1.

- Second, the second flag is opened. The beam collides with the surface and partially sticks on the surface. A drop of QMS intensity occurs, labeled as L_2.

- The sticking probability can be calculated by:

$$S = \frac{L_2}{L_1} \tag{2.4}$$

Fig. 2.2a) shows an example of KW measurements on Potvis. It shows a slowly increasing background, which we account for by fitting and extrapolating the data prior to opening the second flag and by comparison to results when the second flag was not opened at all during experiment. Note that accounting for this modest change in background for the duration of the experiment (on the order of a couple of percent only) is relevant to accurate determination of the time-dependence of sticking. The slow increase in background likely results from variations of the pumping speed of the UHV system and/or a change in the sensitivity of the QMS by exposure to reducing and oxidizing gases, e.g. H_2 and O_2 [14]. Fig. 2.2b) illustrates how we extract an accurate initial sticking coefficient, S_0, from the data in a). We fit the time-dependent sticking obtained through normalizing and inverting the KW trace by a linear functional form through the first couple of seconds and a double exponential functional form when reliable data is available for longer exposures, and extrapolating to the exact time of opening the second flag. This removes the convolution of the QMS partial pressure measurement at 4-5 Hz with the time constant from opening the second flag.

The KW technique used with a single measurement can be applied when the sticking probability, S, is larger than $\sim$0.01-0.03 as the dip in the partial pressure trace that appears when opening the second flag needs to be discernable within the noise-level. To improve our detection limit, the opening and closing of the two flags is computer-controlled with accurate, but variable time intervals for both flags. The sticking probability is measured repeatedly under identical conditions and we average the resulting KW-traces. Hence, we improve our detection limit by (approximately) the square root of the number of repetitions of the measurement. An example of this trick is shown in chapter 4, figure 4.2.

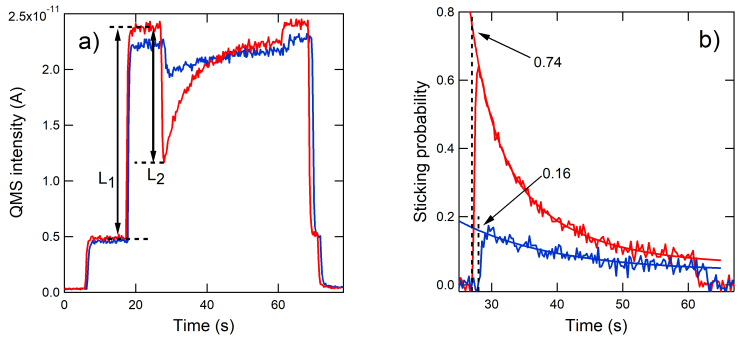

Figure 2.2: a) An example of KW measurements of D_2 on Pt(111) on Potvis. The kinetic energy of D_2 is 0.46 eV. The polar angles between the beam axis and the surface normal are 0° and 50° for the red and blue curves, respectively. The first plateau is cause by the opening of the valve between the two differential pumping stages. b) Examples of the time-dependent sticking and double-exponential fits obtained from normalizing and inverting the KW traces as shown in a).

2.2.3 Time of flight technique

The velocity distribution of the beam can be described by a shifted Maxwell-Boltzmann distribution [15]:

$$P_{vel}(v;T_n) = Av^3\exp(-(v-v_0)^2/\alpha^2) \tag{2.5}$$

where v_0 is the flow velocity, α a measure for the velocity spread, and A a normalization factor. We use time-of-flight (TOF) methods to measure the molecular beam's velocity distribution. The continuous molecular beam is chopped into short pulses by a chopper wheel with a duty cycle of 0.5%. The chopper wheel is spun at a high frequency, resulting in convolution of the TOF distribution with a gating function.

The total measured flight time, t_{total}, is composed of the following contributions:

$$t_{total} = t_{TOF} + \Delta t_{trig} + \Delta t_{elec} + \Delta t_{QMS} \tag{2.6}$$

where t_{TOF} is the flight time of the neutral species from chopper wheel to the QMS ionizer over a distance L. Δt_{trig} captures the offset between the signal of the optical sensor triggering our multi-channel scalar (MCS) card and the center time of release of the gas pulse. Δt_{QMS} captures the flight time of the ionized species from ionizer to the QMS channeltron. Δt_{elec} captures the electronic delay difference for the optical pulse and channeltron pulse to arrive at the MCS card.

Our QMS, with its cross-beam ionizer, is mounted inside a differentially pumped stage, which can be moved by an x, y, z manipulator along the beam axis over a distance, d, of 200 mm on Potvis and 50 mm on Lionfish. By doing so, we vary only L, *i.e.* the flight length of the neutral, hence t_{TOF}. As figure 2.3 shows, through linear extrapolation of t_{total} to L=0 mm, we derive the sum of all other time delays, i.e. $\Delta t_{trig} + \Delta t_{elec} + \Delta t_{QMS}$. These offsetting values are required for fitting procedures in the time-domain, as described below. Simultaneously, the slope in a graph plotting the most probable arrival time for different values of d yields the most probable velocity. This is not identical to v_0, though.

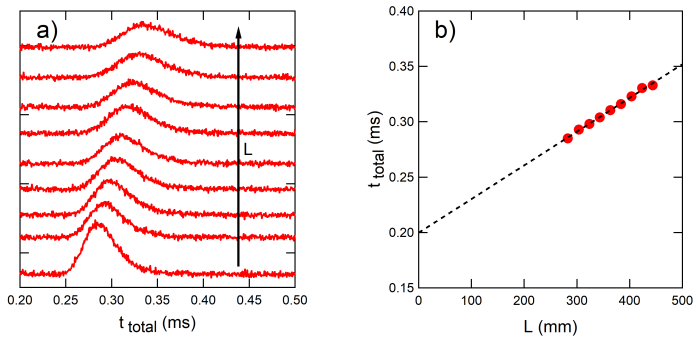

Figure 2.3: a) The TOF spectrum at different L positions. A clear shift of total flight time with increasing flight length, L, is observed b) shows the TOF peak's total flight time versus the flight length L. The intercept with y-axis yields the sum of all other time delays, $\Delta t_{trig} + \Delta t_{elec} + \Delta t_{QMS}$.

To obtain the beam's velocity distribution, we convert equation (2.5) to the time-domain [15]

$$\int P_{vel}(v; T_n) dv = \int g(t; T_n) dt \tag{2.7}$$

Using $v = L/t$ and $dv \sim t^{-2}$ the function can be rewritten as:

$$g(t; T_n) \sim \left(\frac{L}{t}\right)^5 \cdot \exp\left(-\left(\frac{\frac{L}{t} - \frac{L}{t_0}}{\alpha}\right)^2\right) \tag{2.8}$$

The time t in this equation corresponds to the time-of-flight for the neutral species, t_{TOF}. Prior to fitting in the time domain, we correct the measured time, t_{total}, for all delays and off sets as determined by

the procedure described above. Then we fit each TOF spectrum for its specific neutral flight path length, L, taking into account that our density sensitive detector modulates the signal by a factor of $1/v$, hence fitting $g_{dens}(t)$ with a pre-exponential factor proportional to $(L/t)^4$. We also include a gating function by adding nine of the $g_{dens}(t)$ functions, each separated by 3 μs and scaled with the appropriate amplitude. We verify that the flow velocity, v_0, and distribution as characterized by α for spectra taken for identical expansion conditions, but varying L, yield consistent values.

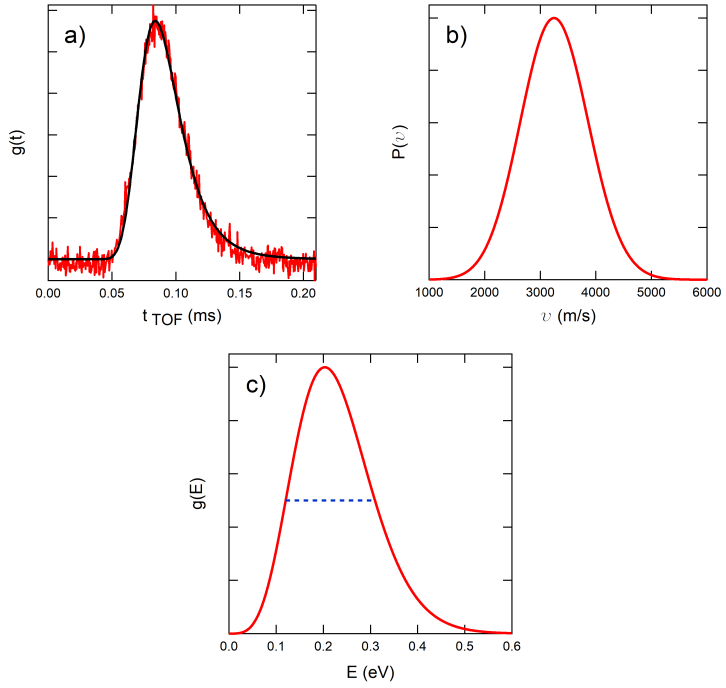

Figure 2.4: a) A typical TOF spectrum (red) and fit (black) in the time domain. b) and c) are the corresponding molecular beam's velocity distribution and energy distribution, respectively. The dashed blue line indicated the full width at half maximum.

We average values for v_0 and α for identical beam conditions and calculate the kinetic energy distribution by converting the velocity distribution to the energy domain:

$$g(E;T_n) = \frac{1}{m\sqrt{2E/m}} P_{vel}(v;T_n) \tag{2.9}$$

where $E = mv^2/2$.

Figure 2.4 shows a typical result of our TOF analysis for a pure D_2 beam. The horizontal dashed line in Fig. 2.4c) shows that the energy width in our beam in a typical experiment is substantial. The nozzle temperatures T_n were calculated from $\langle E_i \rangle = 2.7 \times k_B T_n$ assuming 20% rotational cooling and no vibrational cooling Ref. [16]. Comparison to temperatures measured 10-20 mm downstream the nozzle confirmed that, as expected, in most cases the nozzle temperatures determined from the relation stated above exceed the measured lower bounds, by values in the range 50-470 K. Nozzle temperatures were computed from the accurately determined average translational energies because physical constraints made it impossible to measure the nozzle temperature in our beam machine at the tip of our gas expansion tube. For the measurements reported here, as we noted, the thermocouple was attached 10-20 mm toward a cooling block and, therefore, it provided values significantly lower than the actual expansion temperatures. As the tip of the expansion tube is also hidden from view by heat shields, we could not use an optical pyrometer to measure the actual temperature near the nozzle's orifice. In previous experiments from nearly a decade ago, where the thermocouple was located significantly closer to the tip of a previous design, we measured ∼1800 K as the maximum obtainable temperature for nearly identical heating conditions. This maximum value is consistent with the maximum achieved nozzle temperature we determined from the average translational energies (1744 K).

2.2.4 Temperature programmed desorption

Temperature programmed desorption (TPD) is an experimental technique based on the crystal being heated in time. Species releasing from the surface are monitored.

The rate of thermal desorption is usually described by the Polanyi-Wigner equation:

$$r = -\frac{d\theta}{dt} = \nu(\theta) \cdot \theta^n \cdot exp(-\frac{E_{des}(\theta)}{R \cdot T}) \tag{2.10}$$

where r is the rate of desorption, θ the coverage, ν the coverage-dependent prefactor, E_{des} the coverage-dependent activation energy of desorption, and n the desorption order. In TPD, the temperature,

T, is generally ramped linearly

$$T = T_0 + \beta \cdot t \tag{2.11}$$

Figure 2.5 shows a simulation of TPD spectrum by solving equation 2.10 with the Runge-Kutta method.

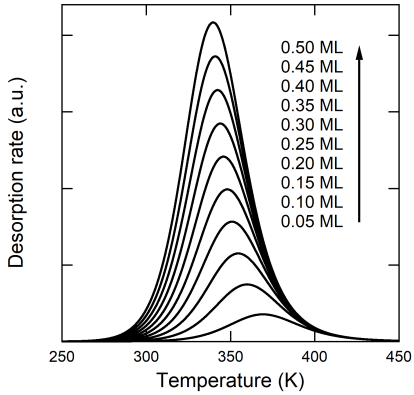

Figure 2.5: A simulation of TPD spectrum for a second order desorption. The parameters are: $E_{des} = 75.0$ kJ/mol, $\nu = 1 \times 10^{11}\ s^{-1}$, n = 2 and $\beta = 2$.

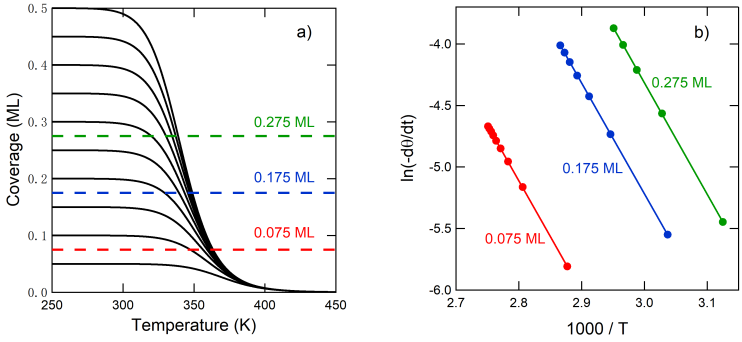

Figure 2.6: The 'complete analysis' of TPD spectrum. Figure a) shows the remaining coverage versus surface temperature. For every selected coverage, there is a pair of (r, T) values for every TPD trace. Figure b) shows the Arrhenius plot of $ln(-d\theta/dt)$ for the selected coverage.

Quantitative analysis of TPD spectra is complex as both E_{des} and ν in equation (2.10) may depend on coverage. By using the so-called 'complete analysis' method[17], we can determine E_{des} and ν for every

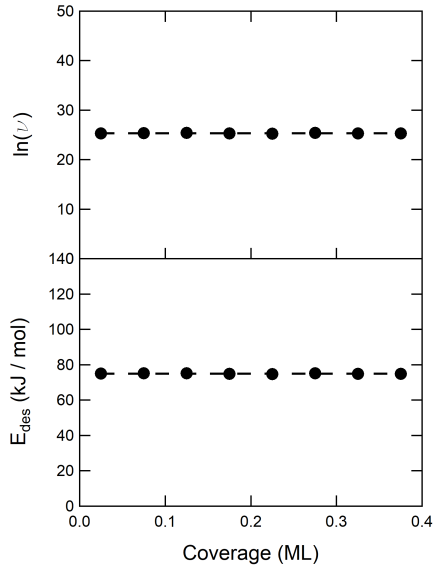

Figure 2.7: The prefactors and desorption energies obtained from 'complete analysis' at different coverage. The E_{des} is (75.00 ± 0.16) kJ/mol. The v is $(1.03 \pm 0.04) \times 10^{11}$ s^{-1}.

coverage. It requires changing equation (2.10) into

$$ln\ r = ln\ \nu(\theta) + n\ ln\ \theta - \frac{E_{des}(\theta)}{RT} \tag{2.12}$$

where the variables are the same as in equation (2.10). An Arrhenius plot of $ln\ r$ versus $1/T$ yields $-E_{des}/R$ as the slope. The intercept for any particular coverage equals $ln\ \nu(\theta) + n\ ln\ \theta$. The complete analysis of TPD spectrum shown in figure 2.5 is illustrated in figure 2.6 and 2.7. The results agree well with our simulation parameters.

2.3 Single crystals

In this thesis two types of single crystals are used. In chapters 3 and 4, we use flat single crystals, like Pt(111), Cu(111) and Cu(211). In chapters 5 and 6, we use a curved Pt(111) single crystal.

Figure 2.8 shows the flat Pt(111) crystal we used in chapter 3. The figure shows how we change the azimuthal angles. From LEED patterns we confirm that at azimuthal angle 0°, figure 2.8a), the azimuthal direction is $[11\bar{2}]$ and at azimuthal angle 30°, figure 2.8b), the

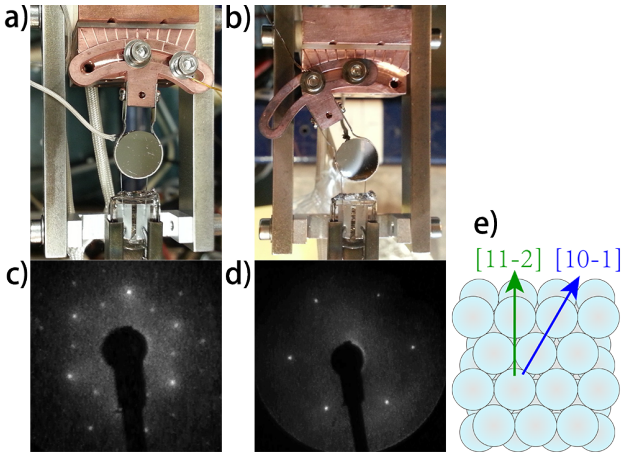

Figure 2.8: Illustration of how we change azimuthal angles on Potvis. Figure a) and b) correspond to azimuthal angle 0° and 30°, respectively. Figure c) and d) are the LEED patterns. Figure e) shows the azimuthal directions. Figure a and c correspond to $[11\bar{2}]$ direction. Figure b and d correspond to $[10\bar{1}]$ direction.

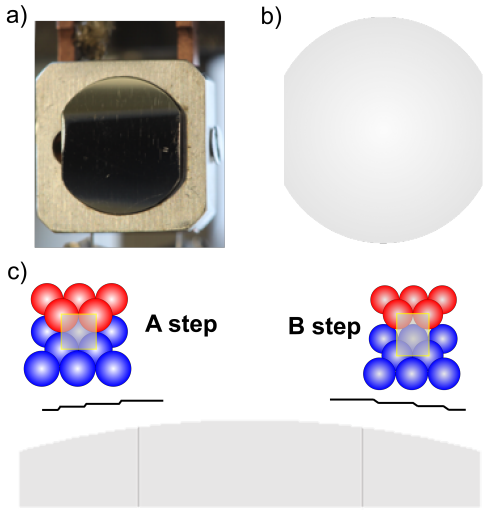

Figure 2.9: Illustration of curved Pt(111) single crystal. Figure a) and b) are the front views. Figure c) is the side view.

azimuthal direction is $[10\bar{1}]$.

Figure 2.9 shows the curved Pt(111) crystal we used in chapter 5 and 6. The crystal is cut and polished to expose a curvature encompassing $\sim 31°$ along the $[11\bar{2}]$ direction with the (111) surface at the apex. On one side the surface is Pt$[N(111) \times (100)]$, also called A step side. On the other side the surface is Pt$[N(111) \times (110)]$, also called

B step side. The length of (111) terrace decreases with distance from apex to both A and B step sides. In figure 2.9b, the height of the crystal is 8 mm and the width of the crystal is 7 mm.